Chemical Engineering Journal 500 (2024) 156997

Contents lists available at ScienceDirect

Chemical Engineering Journal

journal homepage: www.elsevier.com/locate/cej

Enhancing the combustion of silicon nanoparticles via plasma-assisted fluorocarbon surface modification

Emmanuel Vidales Pasos [a], Brandon Wagner [b], Feiyu Xu [a], Yujie Wang [c], Minseok Kim [a], Michael Zachariah [b,c,*], Lorenzo Mangolini [a,b,*]

[a] Mechanical Engineering Department, University of California Riverside, Riverside CA 92521, United States
[b] Materials Science and Engineering Program, University of California Riverside, Riverside CA 92521, United States
[c] Chemical and Environmental Engineering Department, University of California Riverside, Riverside CA 92521, United States

ARTICLE INFO

Keywords:
Coating
Nonthermal plasma
Fluorocarbon
Combustion
Silicon

ABSTRACT

Nanostructured silicon has great potential as an energetic material due to its high energy density, close to that of aluminum; however, its combustion kinetics are strongly affected by the presence of a native oxide layer. As the particle size is reduced, the material behavior is dominated by surface effects, highlighting the need for new approaches to fabricate silicon nanoparticles and precisely control their surface chemistry. Here, we describe the use of low-temperature plasma to nucleate and grow < 10 nm silicon particles. The resulting aerosol is passed through a second plasma reactor, to which a fluorocarbon monomer is supplied. The second plasma initiates the growth of a polymeric shell onto the silicon particles, resulting in a highly conformal coating. Chemical analysis confirms that the polymer shell is compositionally similar to polyvinylidene fluoride (PVDF). We find that the fluorocarbon shell acts as an artificial passivation layer that significantly delays the onset of oxidation in air. In addition, the direct contact between the fluorocarbon shell and silicon core lowers the ignition temperature compared to the physical mixtures of silicon nanoparticles and PVDF. It leads to a higher pressurization rate and a lower combustion time when tested in a combustion cell. This is consistent with the combustion process being initiated by the exothermic interfacial reactions between the silicon core and the fluorocarbon shell. Mass spectroscopy confirms this hypothesis because silicon fluoride is produced only for the core–shell structure, and not for a physical mixture of silicon and PVDF. This study provides an example of a new processing technique capable of controlling the interfacial chemistry of small nanoparticles with beneficial effects on their combustion.

1. Introduction

Metals such as aluminum, magnesium, titanium, boron, silicon, and their alloys are actively investigated as solid-state fuels [1–3]. Their high specific and volumetric energy densities make them attractive candidates for energetic materials. It is well-known that reducing particle size plays a crucial role in improving the kinetics of combustion [4,5]. Increasing the surface-to-volume ratio enhances the contact between the fuel and oxidizer and shortens the diffusion length scales, thereby improving reaction kinetics. However, any improvement from size reduction is countered by the presence of native oxide layers which hinders mass transport and reduces the active content of the material. Several studies have focused on modifying the surface of metal nanoparticles to tune their combustion characteristics [6–9]. Ghildiyal et al. have recently shown that the exothermic reaction between Mg vapor and the native oxide layer of boron particles enhances their combustion [10]. Our group has replaced the native MgO layer on Mg nanoparticles with a silicon shell, achieving a significant reduction in the ignition temperature because of the exothermic interfacial reaction between the particle core and its shell [11]. This structure was realized in a vacuum, before the Mg particles were exposed to air, via plasma-enhanced chemical vapor deposition. The use of plasmas to modify the surface of energetic nanoparticles has recently received significant attention. For instance, hydrogen plasma treatment is effective at partially reducing the surface oxide layer of aluminum particles [12,13]. Miller et al. used an argon plasma to increase the surface hydration of aluminum particles, which correlated with changes in the thermogravimetric analysis [14]. Wagner et al. exposed magnesium nanoparticles to a hydrogen plasma, partially converting them to MgH_2 and inducing a significant reduction in their ignition temperature [15]. It

* Corresponding authors.
E-mail addresses: mrz@engr.ucr.edu (M. Zachariah), lmangolini@engr.ucr.edu (L. Mangolini).

https://doi.org/10.1016/j.cej.2024.156997
Received 7 August 2024; Received in revised form 21 September 2024; Accepted 20 October 2024
Available online 21 October 2024

should be noted that the type of plasma used in these studies is referred to as a low-temperature plasma, i.e. a discharge that can produce a significant density of reactive species while maintaining a low gas temperature. Low thermal loading avoids reactions such as metal hydride decomposition and is therefore crucial for achieving the desired functionality.

This study focuses on silicon as an energetic material. Silicon has high gravimetric (32.4 $kJ{\cdot}g^{-1}$) and volumetric (75.5 $kJ{\cdot}cm^{-3}$) energy density based on its mass and volume when oxidized in air. This is comparable to well-studied energetic materials such as aluminium [16,17]. One barrier to the development of silicon-based energetic materials is the access to small silicon nanopowders with well-defined sizes and size distributions. Our group specializes in low-temperature plasmas to rapidly convert molecular precursors (silane, SiH_4, or chlorosilanes, such as $SiCl_4$) into silicon nanoparticles (SiNPs) [18,19]. These reactors leverage their inherent lack of thermodynamic equilibrium (i.e., electron temperature in the 1–5 eV range, with gas near room temperature) to initiate the nucleation and growth of nanoparticles. Electrostatic stabilization in the plasma slows agglomeration and growth, and the final particle size is typically in the 5–15 nm range, with a narrow distribution (i.e., no particles larger than 20 nm) [20,21]. These properties have already been leveraged for a variety of applications, with plasma-produced Si particles being used in advanced photonics and batteries [22,23]. Our group has already investigated the use of plasma-produced silicon particles in energetic formulations. Ghildiyal et al. used them as an energy filler in mesoparticles composed of aluminum and calcium iodate [24]. Xu et al. found that plasma processing parameters can be tuned to enrich the particle surface with hydrogen, leading to significant gas release and pressure generation upon ignition [25]. In addition, the same process provides a path for controlling the nanoparticle surface and functionality. This can be performed directly in-flight, for instance, by placing two low-temperature plasma reactors in series. The first reactor nucleates and grows the silicon particles, and a chemical precursor is added after the first reactor and before the second plasma to modify the particle surface. For instance, Chaukulkar et al. demonstrated that nonthermal plasmas successfully coat silicon nanoparticles (SiNPs) with amorphous carbon [26]. Yasar-Inceoglu et al. coated SiNPs with a highly conformal polyaniline shell via the gas-phase, plasma-induced polymerization of aniline [27].

In this study, we take advantage of the properties of low-temperature plasmas to produce silicon nanoparticles and coat them in-flight, before air exposure, with a fluorocarbon shell to mitigate the negative effects of native oxide growth while also taking advantage of the oxidative properties of the polymeric shell. Fluorine-containing polymers are attractive supplementary oxidizers because they can react with fuel nanoparticles to exothermically form their respective fluorides [28–30]. We have conducted comprehensive analyses of silicon nanoparticles (SiNPs) samples with and without fluorocarbon (FC) coating using techniques such as transmission electron microscopy (TEM), X-ray diffraction (XRD), scanning electron microscopy coupled with energy-dispersive X-ray spectroscopy (SEM-EDS), Fourier transform infrared spectroscopy (FTIR), and X-ray photoelectron spectroscopy (XPS). These results confirm that a highly conformal FC shell with F/C $\sim$ 1 (i.e. compositionally similar to polyvinylidene fluoride, PVDF) was formed around the crystalline SiNP core. We find that the FC shell significantly improves the chemical stability of the SiNPs against oxidation in air. Ignition measurements performed with either air or potassium perchlorate ($KClO_4$) as oxidizers show a reduced ignition temperature for FC-coated SiNPs compared to both pristine SiNPs and physical mixtures of SiNPs and PVDF. Temperature-jump time-of-flight mass spectrometry (T-Jump TOFMS) results show that SiF_4 is produced during the combustion of the FC-coated SiNPs samples. This confirms that the increased interfacial contact in the core–shell structure, combined with the highly exothermic silicon fluorination reaction, significantly enhances the material combustion. These results show that small nanoparticles can be stabilized against oxidation in air via the application of an artificial passivating shell. They also confirm that low-temperature plasma processing is an effective method for tailoring the performance of energetic materials via the realization of carefully designed nanostructures.

2. Experimental section

2.1. Materials

Hexafluoropropylene (C_3F_6) with a molecular weight of 150.02 g/mol, and polyvinylidene fluoride (PVDF) with a molecular weight of 64.03 g/mol, were acquired from Sigma-Aldrich. HPLC grade water and hexanes (99.9 %) were purchased from Fisher Scientific.

2.2. Plasma processing in-flight of SiNPs

A schematic of the in-flight plasma coating process is shown in Fig. 1. The setup, operating at a constant pressure of 267 Pa (2 Torr), consisted of an initial 1″ quartz tube equipped with two ring copper electrodes linked to a radiofrequency power source delivering 80 W at 13.56 MHZ, which flowed silane (SiH_4) diluted in argon (1.36 % by volume) at 100 sccm. Subsequently, the reactor tube was connected to a 3-way fitting where a mass flow controller supplied an additional stream of 30 sccm of hexafluoropropylene (C_3F_6), which was added to the SiNP aerosol before being directed to a second plasma reactor. The second plasma reactor consists of 1″ quartz tube, where a 40 cm long electrode was connected to a secondary power source delivering 30 W at the same frequency. Nanoparticles were collected by filtering using a fine stainless-steel mesh cloth downstream of the plasma reactor. Before removing the filter, the system was vented slowly for 15 min in an open-air environment to prevent unwanted ignition.

2.3. Characterization of the SiNPs

The size distributions of the FC-coated and uncoated SiNPs were determined using transmission electron microscopy (TEM) by capturing high-resolution transmission electron microscopy (HR-TEM) images and measuring the size of 100 nanoparticles. Imaging was conducted using a Thermo Fisher Scientific Titan Themis 300 instrument. The crystallinity of the particles was assessed by X-ray diffraction (XRD) analysis using a PANalytical Empyrean Series 2 instrument with CuKα radiation (wavelength of 1.5406 Å) and an accelerating voltage of 40 kV within the 2θ range of 15°–90°. The elemental composition of the FC-coated SiNPs was assessed using a ThermoFisher Scientific NNS450, operating at a working distance of 5 mm equipped with an Everhart-Thornley detector (ETD), where 60 scans were processed using Oxford Instruments AztecSynergy software. Chemical characterization was performed using a Thermo Scientific Nicolet iS50 FTIR in conjunction with a Pike Technologies ZnSe attenuated total reflectance (ATR) crystal. The samples were sonicated in chloroform and drop-casted onto an ATR crystal. Using OMNIC software for data collection, 40 scans were averaged from 4000 to 650 cm^{-1} at room temperature. An X-ray photoelectron spectroscopy (XPS) technique was employed to assess the elemental composition of both coated and uncoated nanoparticles. A Kratos AXIS Ultra ^{DLD} system featuring an Al Kα X-ray source and a 165-mm mean radius electron energy hemispherical analyzer was utilized for this purpose.

2.4. Preparation of SiNPs/PVDF and SiNPs/PVDF/$KClO_4$

A composite material consisting of Si and polyvinylidene fluoride (PVDF) was combined with hexanes in a vial and ultrasonicated for 30 min to ensure a homogeneous mixture. The composition of the mixture was controlled to maintain a ratio of 38.3 wt% SiNP (90 % active) and 61.7 wt% PVDF, so that the F/Si ratio is similar to that of the plasma-

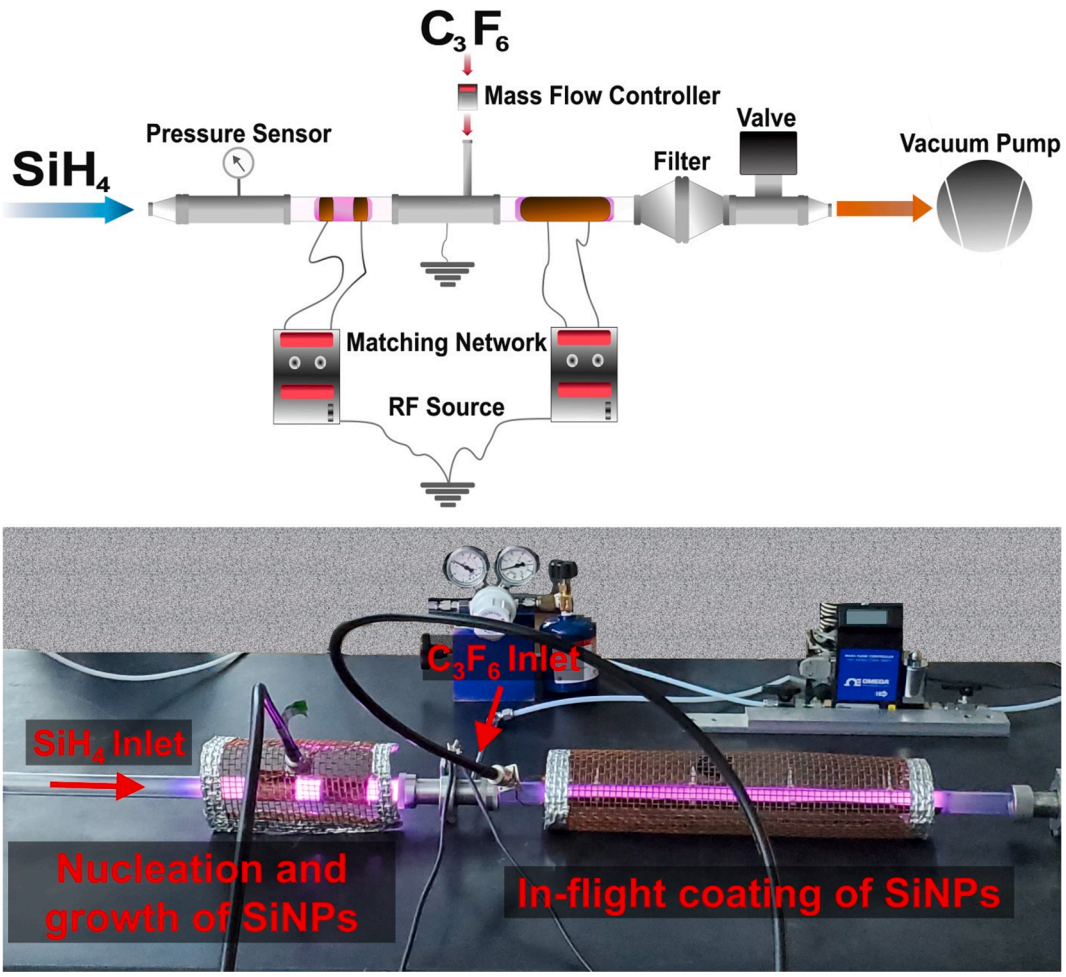

Fig. 1. Schematic of the two capacitively coupled radiofrequency plasma reactors used for synthesizing fluorocarbon-coated and uncoated SiNPs.

processed SiNPs. Subsequently, a small amount of the suspension was coated onto Pt wires. To ensure a PVDF coating on the SiNPs, the coated Pt wires were heated in an oven at 250 °C for 3 h. Pt wires containing the treated SiNPs sample were prepared similarly, but with 3 min of sonication without heating in the furnace.

Three composites were prepared by adding SiNPs, SiNPs/PVDF, and FC-coated SiNPs to $KClO_4$ as oxidizer. The oxidizer amount was adjusted to obtain an equivalence ratio of 1 with silicon. The samples and $KClO_4$ were combined in hexanes via ultrasonication to ensure a homogeneous mixture. The composites were dried for 24 h under ambient conditions to generate thermite powders. For completeness, we show estimates of the enthalpy of reactions in the Supplementary Information document, for the cases of SiNPs and FC-coated SiNPs combusted with $KClO_4$.

2.5. Temperature-jump time-resolved mass spectrometry and ignition

Analysis of the reaction at a high heating rate was carried out using T-Jump time of flight (TOFMS). Further details on the T-jump TOFMS can be found in previous studies [31,32]. The analyte was coated on a 70 μm Pt wire which is resistively heated to a temperature of approximately 1300 K at a rate of 105 K/s, while collecting time-resolved mass spectra data every 100 μs. The temperature of the wire during heating was calculated based on the acquired voltage and current data using the Callendar-Van Dusen equation. For the ignition characterization, the samples were ignited inside a chamber filled with air at 1 atm. The ignition delay time was determined from the obtained video after triggering the heating process on the Pt wire at 100,000 fps with an exposure of 9.57 us, enabling the estimation of the ignition time which could be mapped to temperature. A pressure cell test was performed to further analyze the reactivity of the FC-coated particles mixed with PVDF. The samples were mixed in hexanes and allowed to dry to obtain 25 mg of loose thermite powder, which was placed in a constant-volume combustion cell and ignited using a resistive heating nichrome wire [33,34]. The experimental setup involved placing the samples in a constant-volume cell (~20 cm^3) at atmospheric pressure. The nichrome wire was resistively heated to ignite the sample, leading to self-propagation of the sample in the chamber. An oscilloscope recorded the pressure and optical signal simultaneously, whereas a high-frequency pressure transducer captured the time-dependent pressure signal. The pressurization rate, determined by dividing the peak pressure by the rise time of the pressure signal, functions as a relative measure of reactivity and shows a documented association with flame propagation speeds. The burning time was characterized by the optical emission signal's full width at half maximum (FWHM). Three runs were conducted for each sample to determine the average pressurization and burn characteristics. Differential scanning calorimetry (DSC) was performed on a Netzsch STA 449 F3 Jupiter thermal analyzer from room temperature to 1000 °C at a ramp rate of 10 K min^{-1} in Ar.

3. Results and discussion

3.1. Characterizations of SiNPs and FC-coated SiNPs

The size distributions and morphologies of the SiNPs and FC-coated SiNP particles were determined by high-resolution TEM. Both samples exhibited a spherical morphology with a crystalline structure, as shown

in Fig. 2a-b. Fig. 2a illustrates SiNPs surrounded by a native oxide layer grown at room temperature. In contrast, Fig. 2b shows an FC-coated SiNP, suggesting that there is an amorphous shell surrounding the particle core. A STEM-EDS map of the in-flight coated material is shown in Figure S1, confirming the presence of fluorine in the shell. The size distribution derived from the analysis of 100 particles is plotted in Fig. 2c-d. The SiNPs exhibit an average diameter of 5.65 nm including an oxide layer with a thickness of 0.8 nm. The FC-coated SiNPs particles have an average size of 7.23 nm. The crystallinity of the SiNP samples was verified using X-ray diffraction (XRD). Fig. 2e shows the XRD patterns with peaks at ~ 28°, ~47°, and ~ 56° corresponding to the (111), (220), and (311) planes of Si, respectively [35]. The same pattern can be observed for the FC-coated SiNPs, suggesting that no carbonization of the silicon core occurred during exposure to the second plasma.

The elemental composition of the FC-coated SiNPs was analyzed using SEM-EDS. The average atomic percentages (at.%), obtained from the 60 measurements, indicate that C, F, and Si constitute 36.35 ± 4.25 at.%, 36.68 ± 3.54 at.%, and 26.97 ± 3.68 at.%, respectively, confirming the same F/C ~ 1 found in PVDF. The balanced presence of F and C can lead to both elements being fully utilized during combustion, resulting in a more stable chemical reaction and lower ignition temperature, as demonstrated by Li et al. in their analysis of Al/PVDF [36].

The effect of RF power and C_3F_6 flow rate on the elemental composition (F/C, F/Si, and C/Si ratios) of the FC-coated SiNPs is summarized in the supplementary information, in Figure S2. We find that varying the power in the second plasma with a constant C_3F_6 flow rate of 30 sccm does not affect the F/C ratio, as determined via SEM-EDS and XPS analysis. An increase in power results in a decrease in the F/Si and C/Si ratios, consistent with a thinner polymeric shell. An increase in the C_3F_6 flow rate from 25 sccm to 90 sccm (see Figure S3) results in a decrease in the F/C, F/Si and C/Si ratios, also consistent with a decrease in shell thickness. While these trends deserve further investigation, the overall weak dependence of the elemental composition over process parameters is consistent with a slow surface grafting reaction, with competing pathways being present. For instance, an increase in RF power supplied to the second plasma likely results in increased formation of atomic hydrogen, with hydrogen being produced in the first plasma during the nanoparticle nucleation and growth from silane. Studies related to plasma deposition of fluorocarbon coatings have shown that H atoms can scavenge fluorine atoms [37]. Hydrogen is also well-known to decrease the rate of plasma-induced polymerization of unsaturated hydrocarbons [38].

Additional details of the chemical composition of the SiNPs, FC-

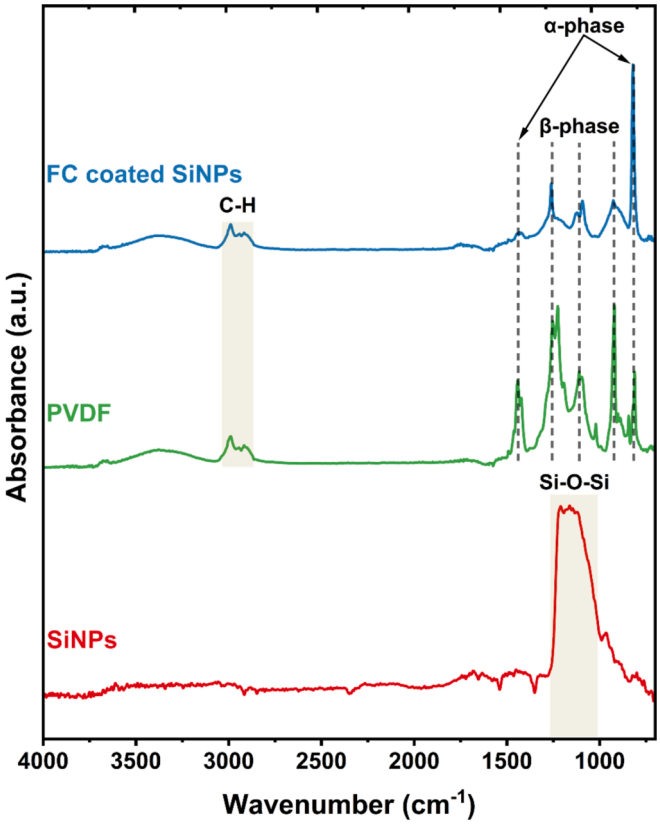

Fig. 3. Fourier transform infrared (FTIR) spectra of SiNPs, PVDF, and FC-coated SiNPs. The PVDF- and FC-coated SiNPs shared peaks assigned to the C-H, α-, and β-phases of PVDF.

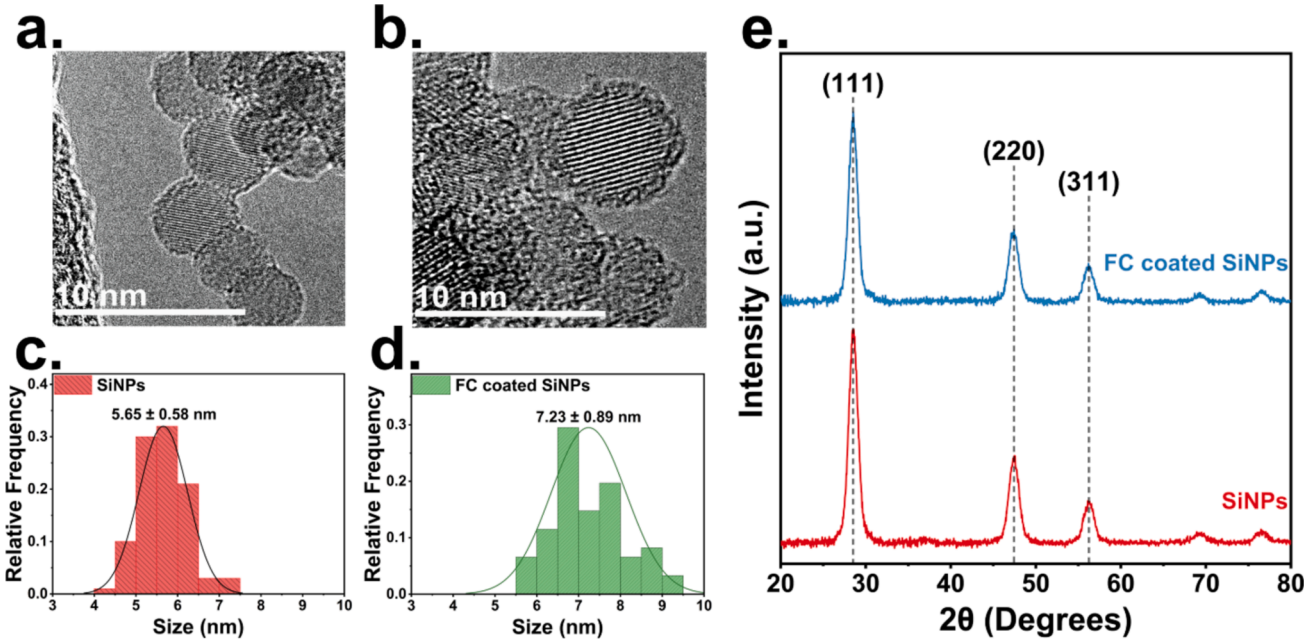

Fig. 2. (a) High-resolution images of SiNPs and (b) FC-coated SiNPs. Size distributions of (c) SiNPs and (d) FC-coated SiNPs (d) obtained from STEM. (e) XRD patterns of FC-coated and uncoated SiNPs. Diffraction peaks were observed at the same positions in both the cases.

coated SiNPs, and PVDF were collected by Fourier transform infrared (FTIR) analysis, as shown in Fig. 3. The SiNPs show a broad peak in the 1200–1080 cm^{-1} range due to silicon oxidation [39]. The PVDF and FC-coated SiNPs show similarities in the absorption of C-H stretching (~2850–3000 cm^{-1}) and peaks which are also observed for the α- and β-phases of PVDF [40,41]. Peaks in the α-phase are observed at ~ 762 cm^{-1} (stretching for CF_2 + CCC) and ~ 1211 cm^{-1} (stretching for CF_2 + wagging for CH_2), whereas peaks for the β-phase are observed at ~ 879 cm^{-1} (stretching for C-C + CF_2), ~1073 cm^{-1} (stretching for C-C + wagging for CF_2 + CH_2), and ~ 1401 cm (wagging for CH_2 − stretching for C-C) [42,43]. Overall, the combination of EDS and FTIR confirms that the fluorocarbon coating applied by the plasma onto the SiNPs is similar to PVDF. It is therefore appropriate to use physical mixtures of uncoated SiNPs and PVDF as control samples, to further investigate the reactivity of the core–shell FC-coated SiNPs.

X-ray Photoelectron Spectroscopy (XPS) was used to determine the elemental composition of the shells around the SiNPs. For FC-coated SiNPs, we can reasonably assume that the results contain information on both the surface and bulk compositions because their size is similar to the photoelectron penetration depth (approximately 2–5 nm) [44]. Fig. 4a-c display the elemental composition of FC-coated SiNPs after one week of synthesis, confirming the presence of Si, C, F, and O. For completeness, the Si 2p, C 1 s, and F 1 s signals were deconvoluted using the Gaussian profiles. The Si 2p spectrum is shown in Fig. 4a, with contributions at 99.7 eV corresponding to Si-Si, 100.8 eV for Si-C, and 103.5 eV for Si-O_2 [45]. The C 1 s spectrum reveals a peak at 283.4 eV (C-Si), 286.7 eV (C-CF_x), 291.4 eV (C-F_2), and 293.5 eV (C-F_3), as shown in Fig. 4b, consistent with previous studies [46–49]. The presence of C-F bonding is confirmed in the F 1 s spectrum because of a dominant peak at 688.9 eV (F-C), whereas the F-O and F-Si peaks are at 692.1 eV and 686.9 eV respectively [46,50], as illustrated in Fig. 4c. These spectra suggest that carbon serves as a linkage between fluorine and silicon, with negligible direct bonding of F to Si.

To study the aging characteristics of FC-coated and uncoated SiNPs, we compared the changes in the elemental composition over a period of 4 weeks, as shown in Fig. 5. The oxygen content of the FC-coated SiNPs after one week from production showed a 15.8 at.% of oxygen content. After four weeks, the O content was 24.4 at.%, which was lower than that of SiNPs without any shell (45.4 at.%) after the same period (see Figure S4). These findings suggest that the in-flight coating with a fluorocarbon shell is effective at significantly slowing down oxidation in air.

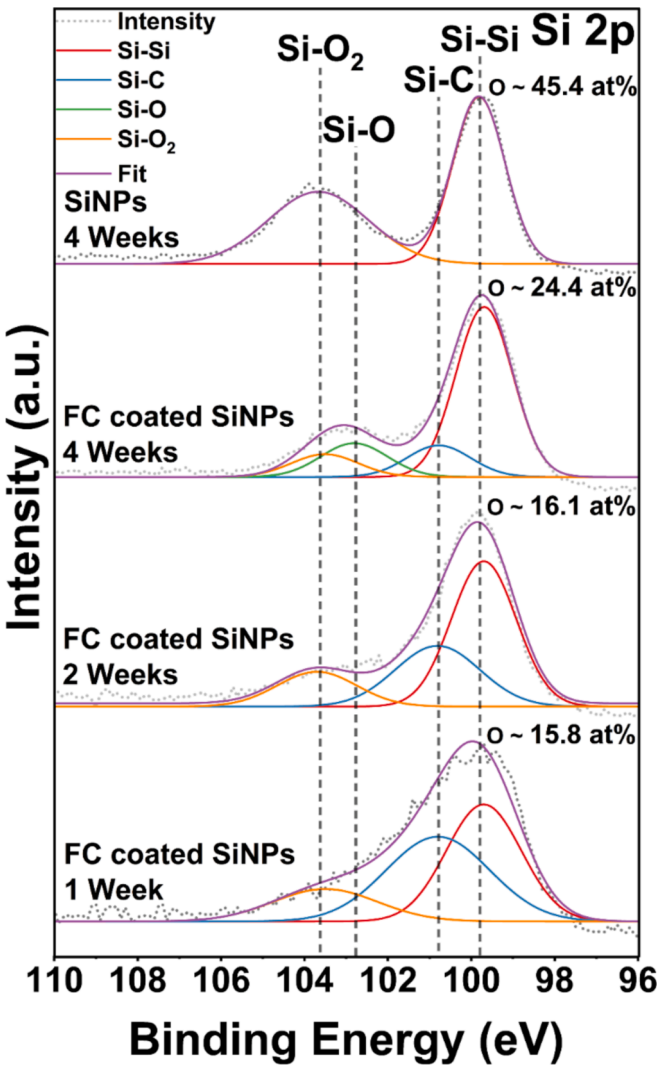

Fig. 5. XPS scans were conducted for Si 2p on the SiNPs, SiNPs/PVDF, and FC-coated SiNPs. The oxidation evolution of the FC-coated SiNPs was compared with that of the SiNPs and SiNPs/PVDF over a period of four weeks.

3.2. Combustion of SiNPs and FC-coated SiNPs

T-jump measurements for SiNPs, physically mixed SiNPs/PVDF, and FC-coated SiNPs in air, with and without the addition of $KClO_4$ as an oxidizer, were conducted to compare their ignition temperatures and shed more light into the reaction pathway. The ignition temperature was determined through the analysis of high-speed image recordings in three separate trials in air, revealing that the ignition delay of the FC-coated SiNPs (~1.6 ms) was half that of its PVDF/SiNPs counterpart (~3.4 ms). T-jump TOFMS was used to analyze the gaseous reaction products released from the ignition in air of SiNPs, SiNPs/PVDF, and FC-coated SiNPs. Fig. 6a shows the T-jump TOFMS results for the combustion products, including the pure PVDF. The mass-to-charge (m/z) peaks at

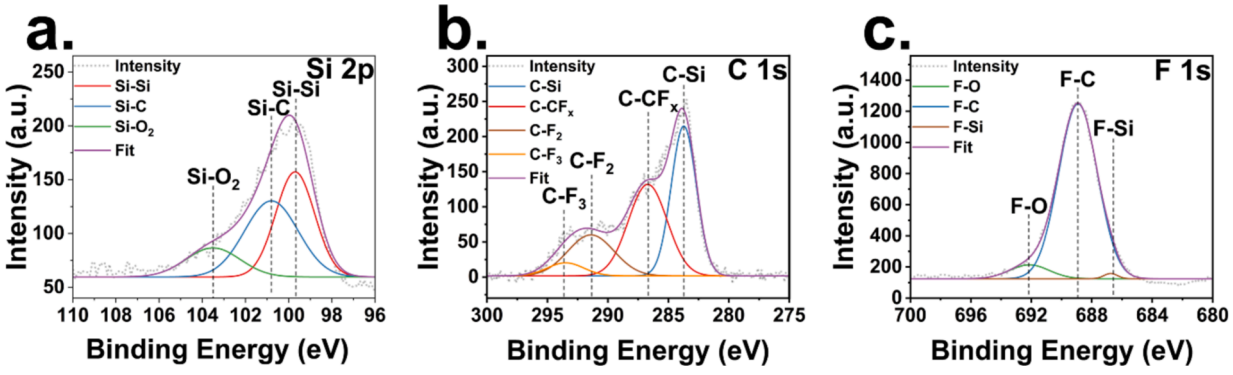

Fig. 4. XPS scans of Si 2p, C 1 s, and F 1 s for FC-coated SiNPs.

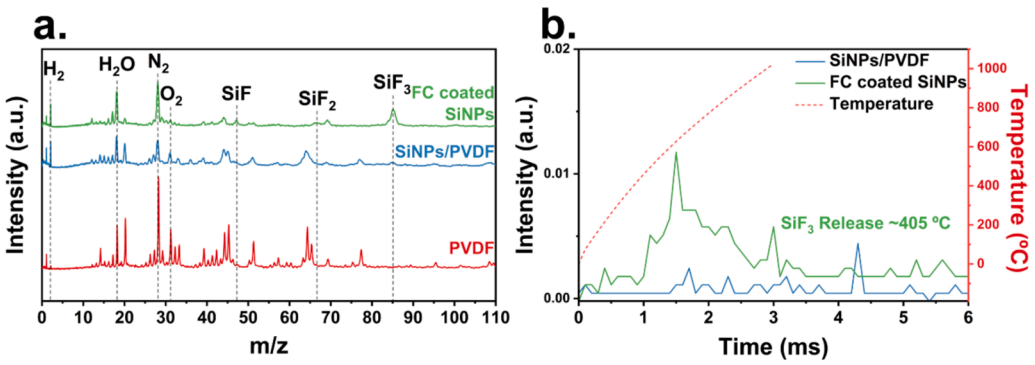

Fig. 6. (a) Full spectra of T-jump-TOFMS of FC-coated SiNPs, SiNPs/PVDF, and pure PVDF when ignited in air, showing decomposition and gas-phase products. (b) Timing and thermal profiles for the detection of SiF_4. The samples were exposed to air at 1 atm inside the chamber, without mixing with $KClO_4$.

18 and 28 correspond to water (H_2O) and nitrogen (N_2). The SiF_3 peak is due to the presence of SiF_4 because to the nature of the TOFMS method. SiF_4 undergoes ionization into SiF_3^+ and F by electron impact because of the dominant dissociative ionization pathway [51]. The FC-coated SiNPs exhibited a peak at $m/z = 66$ (SiF_2) and significant emission of SiF_3 ($m/z = 85$). Fig. 6b shows that SiF_3 began to be released after ~ 0.9 ms at 405 °C while the SiNPs/PVDF mixture did not release silicon fluoride. The ignition temperature for FC-coated SiNPs in air was ~ 620 °C. This is consistent with a condensed-phase chemical reaction between the silicon core and the fluorocarbon shell. We should point out that PVDF decomposes in the 400 °C-500 °C range, with the decomposition proceeding via scission of the C-H bond and subsequent formation of HF [52]. This then leads to the reaction with the silicon core and the release of fluorinated silicon species. Differential Scanning Calorimetry (DSC) measurements further support this mechanism. Figure S5 shows the DSC measurement for the FC-coated SiNPs. A clear exothermic peak is observed with an onset at 400 °C and peaking at 574 °C, consistent with the exothermic reaction between silicon and fluorine and with the release of SiF_3 that we observe in the T-jump TOFM measurements.

Further investigation of the combustion of SiNPs, SiNPs/PVDF, and FC-coated SiNPs, with the addition of potassium perchlorate ($KClO_4$) as an oxidizer, was performed using the same tools described above. The images in Fig. 7a-c show high-speed videos capturing the ignition processes of three samples. T-jump TOFMS analysis revealed noticeable variations in the outcomes of the ignition process among the diverse samples, with clear signals from SiF_2 and SiF_3 only for the case of the FC-coated sample, as shown in Fig. 7d. The ignition of SiNPs/$KClO_4$ began at 580 °C (+1.462 ms). For SiNPs/PVDF/$KClO_4$, ignition started at 595 °C (+1.529 ms). Both of these temperatures are close to the release temperature of O_2 from $KClO_4$, which is ~ 592 °C [53]. In contrast, the FC-coated SiNPs/$KClO_4$ ignited at 510 °C (+1.265 ms). In Fig. 7e we compare the ignition temperature of these samples with the O_2 release temperature from $KClO_4$. The FC-coated SiNPs exhibit a lower ignition temperature (~510 °C) than their counterparts and ignite below the $KClO_4$ decomposition temperature. Figure S6 shows the SiF_4 and O_2 release profiles from T-jump/TOFMS for FC-coated SiNPs. The release of O_2 overlaps with the release of SiF_3 and is in good agreement with the sample ignition temperature. Ignition and early decomposition of $KClO_4$ are likely induced by the highly exothermic, condensed phase silicon fluorination reaction which starts around 400 °C. The physical mixture of SiNPs and PVDF does not show the same behavior. We attribute this to both the poor contact between PVDF and SiNPs, as opposed to the highly conformal case of the FC-coated SiNPs, and to the inevitable presence of a native oxide shell around the silicon core. The presence of a conformal fluorocarbon shell limits the growth of the native oxide and facilitates the exothermic silicon fluorination reaction. Pressure cell experiments were conducted to compare the pressurization rates and peak pressures of the FC-coated SiNPs and the physical mixtures of SiNPs and PVDF, when blended with $KClO_4$. The results are shown in Fig. 7f-h. The findings show that FC-coated SiNPs perform better than SiNPs/PVDF because they have a significantly higher pressurization rate and shorter burn time.

Based on the above discussion, Fig. 8 summarizes the reaction mechanism of the FC-coated SiNPs. Upon heating, the FC coating interacts with the silicon core resulting in a condensed-phase, exothermic reaction that coincides with the release of SiF_x volatile species. The localized release of energy and the disruption of the fluorocarbon protective layer exposes the Si core to the oxidizer, enhancing the combustion process and leading to increased pressurization rate and decreased burn time. The proposed core–shell structure enhances the silicon combustion because of (1) the absence of a native oxide layer that hinders further oxidation and (2) the direct contact between the silicon core and the fluorocarbon shell, which accelerates the rate of exothermic interfacial reactions.

4. Conclusion

We have described a gas-phase process for the nucleation, growth, and immediate passivation of silicon nanoparticles with sizes below 10 nm. We leverage the properties of low-temperature plasmas to obtain particles with a narrow size distribution and a highly conformal fluorocarbon coating. XPS and FTIR data indicate that the fluorocarbon coating is chemically similar to PVDF. This structure provides two main advantages compared to physical mixtures of silicon nanoparticles and PVDF. First, the coating is applied in flight, before exposure to air. The FC coating acts as an excellent barrier against oxidation, with minimal oxide growth even 4 weeks after exposure to air. In addition, the close contact between the fluorocarbon and the silicon particles has major consequences on their combustion. We observe a significantly reduced ignition temperature, higher pressurization rate, and lower combustion time when compared to mixtures of silicon and PVDF. SiF_3 is detected in the Tjump/TOFMS measurements, consistent with a combustion process that is jump-started by the interfacial reaction between the unoxidized silicon core and the fluorocarbon shell. Overall, our work confirms that precise control of surface chemistry is needed for nanostructured solid-state fuels and that this is achievable via novel processing techniques such as the plasma process used here.

CRediT authorship contribution statement

Emmanuel Vidales Pasos: Methodology, Investigation, Formal analysis. **Brandon Wagner:** Formal analysis, Data curation. **Feiyu Xu:** Project administration, Investigation, Data curation. **Yujie Wang:** Formal analysis, Data curation. **Minseok Kim:** Methodology, Investigation, Data curation. **Michael Zachariah:** Writing – review & editing, Supervision. **Lorenzo Mangolini:** Writing – review & editing, Supervision, Project administration, Data curation.

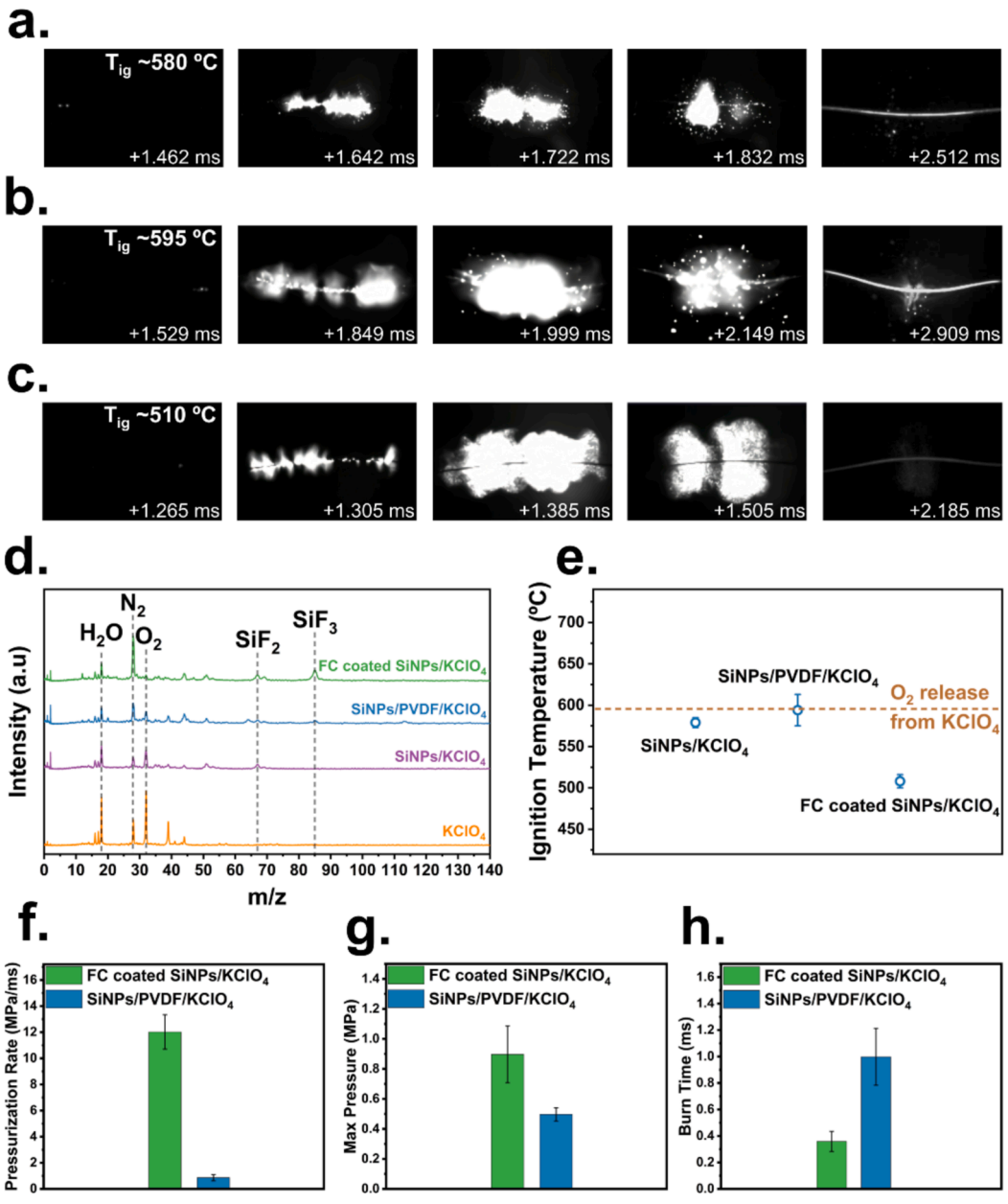

Fig. 7. High-speed camera images of ignition for (a) SiNPs/$KClO_4$,(b) SiNPs/PVDF/$KClO_4$, and (c) FC-coated SiNPs/$KClO_4$. (d) Full spectra of FC-coated Si-$KClO_4$, Si-PVDF-$KClO_4$, Si-$KClO_4$, and $KClO_4$. (e) Analysis of ignition temperature in relation to the release of oxygen for SiNPs/$KClO_4$, SiNPs/PVDF/$KClO_4$, and FC-coated SiNPs/$KClO_4$. Comparison of pressure cell results between FC-coated SiNPs/$KClO_4$ and SiNPs/PVDF/$KClO_4$ for (f) pressurization rate, (g) maximum pressure, and (h) burn time.

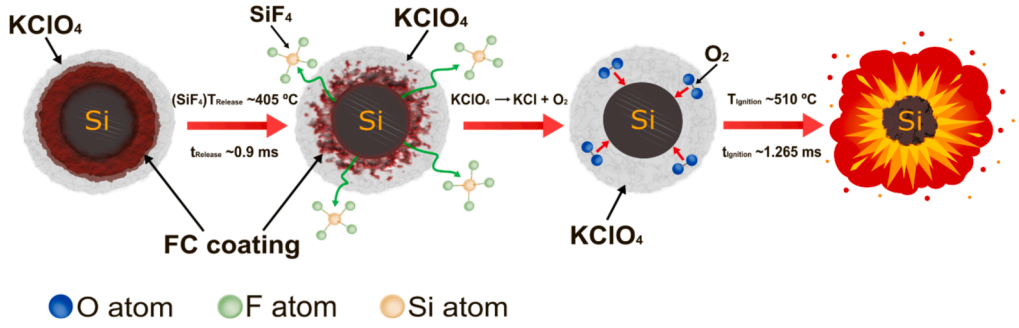

Fig. 8. Schematic representation of the hypothesized reaction mechanism of FC coated SiNPs.

Declaration of competing interest

The authors declare that they have no known competing financial interests or personal relationships that could have appeared to influence the work reported in this paper.

Acknowledgments

This work was primarily supported by the Defense Threat Reduction Agency (DTRA) Materials Science in Extreme Environments University Research Alliance (MSEE-URA). The authors also want to acknowledge support from the Office of Naval Research (ONR). Electron microscopy was performed on a FEI TitanThemis 300 in the Central Facility for Advanced Microscopy and Microanalysis (CFAMM) at UC Riverside.

Appendix A. Supplementary data

Supplementary data to this article can be found online at https://doi.org/10.1016/j.cej.2024.156997.

Data availability

Data will be made available on request.

References

[1] D. Sundaram, V. Yang, R.A. Yetter, Metal-based nanoenergetic materials: synthesis, properties, and applications, Prog. Energy Combust. Sci. 61 (2017) 293–365, https://doi.org/10.1016/j.pecs.2017.02.002.
[2] Y.F. Ivanov, M.N. Osmonoliev, V.S. Sedoi, V.A. Arkhipov, S.S. Bondarchuk, A. B. Vorozhtsov, A.G. Korotkikh, V.T. Kuznetsov, Productions of ultra-fine powders and their use in high energetic compositions, Propellants Explos. Pyrotech. 28 (6) (2003) 319–333, https://doi.org/10.1002/prep.200300019.
[3] E.L. Dreizin, M. Schoenitz, Mechanochemically prepared reactive and energetic materials: a review, J. Mater. Sci. 52 (20) (2017) 11789–11809, https://doi.org/10.1007/s10853-017-0912-1.
[4] R.A. Yetter, G.A. Risha, S.F. Son, Metal particle combustion and nanotechnology, Proceedings of the Combustion Institute 32(2) (2009) 1819–1838, https://doi.org/10.1016/j.proci.2008.08.013.
[5] Y. Huang, G.A. Risha, V. Yang, R.A. Yetter, Effect of particle size on combustion of aluminum particle dust in air, Combust. Flame 156 (1) (2009) 5–13, https://doi.org/10.1016/j.combustflame.2008.07.018.
[6] L. Guo, W. Song, C. Xie, X. Zhang, M. Hu, Characterization and thermal properties of carbon-coated aluminum nanopowders prepared by laser-induction complex heating in methane, Mater. Lett. 61 (14) (2007) 3211–3214, https://doi.org/10.1016/j.matlet.2006.11.035.
[7] P.P.K. Agarwal, E.J. Haley, T. Matsoukas, Synthesis and characterization of energetic aluminum boride particles coated with reactive plasma nanofilms, ACS Applied Engineering Materials 2 (2) (2024) 467–477, https://doi.org/10.1021/acsaenm.3c00762.
[8] M.J. Meziani, C.E. Bunker, F. Lu, H. Li, W. Wang, E.A. Guliants, R.A. Quinn, Y.-P. Sun, Formation and properties of stabilized aluminum nanoparticles, ACS Appl. Mater. Interfaces 1 (3) (2009) 703–709, https://doi.org/10.1021/am800209m.
[9] D.W. Kim, K.T. Kim, D.-U. Lee, S.-H. Jung, D.Y. Yang, J. Yu, Influence of poly (vinylidene fluoride) coating layer on exothermic reactivity and stability of fine aluminum particles, Appl. Surf. Sci. 551 (2021) 149431, https://doi.org/10.1016/j.apsusc.2021.149431.
[10] P. Ghildiyal, F. Xu, A. Rojas, Y. Wang, M. Chowdhury, P. Biswas, S. Herrera, R. Abbaschian, M.R. Zachariah, Magnesium-enhanced reactivity of boron particles: role of Mg/B2O3 exothermic surface reactions, Energy Fuel 37 (4) (2023) 3272–3279, https://doi.org/10.1021/acs.energyfuels.2c02347.
[11] B. Wagner, P. Ghildiyal, P. Biswas, M. Chowdhury, M.R. Zachariah, L. Mangolini, In-flight synthesis of core-shell Mg/Si–SiOx particles with greatly reduced ignition temperature, Adv. Funct. Mater. 33 (21) (2023) 2212805, https://doi.org/10.1002/adfm.202212805.
[12] P.P.K. Agarwal, T. Matsoukas, Engineered surface chemistry and enhanced energetic performance of aluminum nanoparticles by nonthermal hydrogen plasma treatment, Nano Lett. 23 (12) (2023) 5541–5547, https://doi.org/10.1021/acs.nanolett.3c00908.
[13] K.K. Miller, J.L. Gottfried, S.D. Walck, M.L. Pantoya, C.-C. Wu, Plasma surface treatment of aluminum nanoparticles for energetic material applications, Combust. Flame 206 (2019) 211–213, https://doi.org/10.1016/j.combustflame.2019.04.042.
[14] K.K. Miller, I. Shancita, S.K. Bhattacharia, M.L. Pantoya, Surface modifications of plasma treated aluminum particles and direct evidence for altered reactivity, Mater. Des. 210 (2021) 110119, https://doi.org/10.1016/j.matdes.2021.110119.
[15] B. Wagner, M. Kim, M. Chowdhury, E. Vidales Pasos, K. Hizon, P. Ghildiyal, M.R. Zachariah, L. Mangolini, Enhancing the combustion of magnesium nanoparticles via low-temperature plasma-induced hydrogenation, ACS Applied Materials & Interfaces 15(44) (2023) 51639-51649. 10.1021/acsami.3c12696.
[16] M. Comet, C. Martin, F. Schnell, D. Spitzer, Nanothermites: a short review factsheet for experimenters, present and future challenges, Propellants, Explosives, Pyrotechnics 44 (1) (2019) 18–36, https://doi.org/10.1002/prep.201800095.
[17] A. Plummer, V. Kuznetsov, T. Joyner, J. Shapter, N.H. Voelcker, The burning rate of energetic films of nanostructured porous silicon, Small 7 (23) (2011) 3392–3398, https://doi.org/10.1002/smll.201101087.
[18] T. Lopez, L. Mangolini, On the nucleation and crystallization of nanoparticles in continuous-flow nonthermal plasma reactors, J. Vac. Sci. Technol. B 32 (6) (2014) 061802, https://doi.org/10.1116/1.4899206.
[19] O. Yasar-Inceoglu, L. Mangolini, Characterization of Si–Ge alloy nanocrystals produced in a non-thermal plasma reactor, Mater. Lett. 101 (2013) 76–79, https://doi.org/10.1016/j.matlet.2013.03.080.
[20] L. Mangolini, E. Thimsen, U. Kortshagen, High-yield plasma synthesis of luminescent silicon nanocrystals, Nano Lett. 5 (4) (2005) 655–659.
[21] U.R. Kortshagen, R.M. Sankaran, R.N. Pereira, S.L. Girshick, J.J. Wu, E.S. Aydil, Nonthermal plasma synthesis of nanocrystals: fundamental principles, materials, and applications, Chem. Rev. 116 (18) (2016) 11061–11127, https://doi.org/10.1021/acs.chemrev.6b00039.
[22] J. Schwan, B. Wagner, M. Kim, L. Mangolini, Controlled growth of silicon particles via plasma pulsing and their application as battery material, J. Phys. D Appl. Phys. 55 (9) (2021) 094002, https://doi.org/10.1088/1361-6463/ac3867.
[23] K. Wang, R.P. Cline, J. Schwan, J.M. Strain, S.T. Roberts, L. Mangolini, J.D. Eaves, M.L. Tang, Efficient photon upconversion enabled by strong coupling between silicon quantum dots and anthracene, Nat. Chem. (2023), https://doi.org/10.1038/s41557-023-01225-x.
[24] P. Ghildiyal, X. Ke, P. Biswas, G. Nava, J. Schwan, F. Xu, D.J. Kline, H. Wang, L. Mangolini, M.R. Zachariah, Silicon nanoparticles for the reactivity and energetic density enhancement of energetic-biocidal mesoparticle composites, ACS Appl. Mater. Interfaces 13 (1) (2021) 458–467, https://doi.org/10.1021/acsami.0c17159.
[25] F. Xu, G. Nava, P. Biswas, I. Dulalia, H. Wang, Z. Alibay, M. Gale, D.J. Kline, B. Wagner, L. Mangolini, M.R. Zachariah, Energetic characteristics of hydrogenated amorphous silicon nanoparticles, Chem. Eng. J. 430 (2022) 133140, https://doi.org/10.1016/j.cej.2021.133140.
[26] R.P. Chaukulkar, K. de Peuter, P. Stradins, S. Pylypenko, J.P. Bell, Y. Yang, S. Agarwal, Single-step plasma synthesis of carbon-coated silicon nanoparticles, ACS Appl. Mater. Interfaces (2014), https://doi.org/10.1021/am504913n.
[27] O. Yasar-Inceoglu, L. Zhong, L. Mangolini, Core/shell silicon/polyaniline particles via in-flight plasma-induced polymerization, J. Phys. D Appl. Phys. 48 (31) (2015) 314009.
[28] S. Huang, M. Pan, S. Deng, Y. Jiang, J. Zhao, B. Levy-Wendt, S.K.Y. Tang, X. Zheng, Modified micro-emulsion synthesis of highly dispersed Al/PVDF composites with enhanced combustion properties, Adv. Eng. Mater. 21 (5) (2019) 1801330, https://doi.org/10.1002/adem.201801330.
[29] M.C. Rehwoldt, H. Wang, D.J. Kline, T. Wu, N. Eckman, P. Wang, N.R. Agrawal, M. R. Zachariah, Ignition and combustion analysis of direct write fabricated aluminum/metal oxide/PVDF films, Combust. Flame 211 (2020) 260–269, https://doi.org/10.1016/j.combustflame.2019.08.023.
[30] C. Zhang, H. Mao, R. Cui, X. Zhang, J. Yang, J. Ji, X. Zhou, Electrospinning preparation, energetic characteristics and reaction mechanism of corrosion-resistant Si@PVDF nanostructured energetic films, Combust. Flame 237 (2022) 111887, https://doi.org/10.1016/j.combustflame.2021.111887.
[31] W. Zhou, J.B. DeLisio, X. Wang, M.R. Zachariah, Reaction mechanisms of potassium oxysalts based energetic composites, Combust. Flame 177 (2017) 1–9, https://doi.org/10.1016/j.combustflame.2016.05.024.
[32] L. Zhou, N. Piekiel, S. Chowdhury, M.R. Zachariah, T-Jump/time-of-flight mass spectrometry for time-resolved analysis of energetic materials, Rapid Commun. Mass Spectrom. 23 (1) (2009) 194–202, https://doi.org/10.1002/rcm.3815.
[33] K.T. Sullivan, N.W. Piekiel, S. Chowdhury, C. Wu, M.R. Zachariah, C.E. Johnson, Ignition and combustion characteristics of nanoscale Al/AgIO3: a potential energetic biocidal system, Combust. Sci. Technol. 183 (3) (2010) 285–302, https://doi.org/10.1080/00102202.2010.496378.
[34] F. Xu, P. Biswas, G. Nava, J. Schwan, D.J. Kline, M.C. Rehwoldt, L. Mangolini, M. R. Zachariah, Tuning the reactivity and energy release rate of I2O5 based ternary thermite systems, Combust. Flame 228 (2021) 210–217, https://doi.org/10.1016/j.combustflame.2020.12.047.
[35] T. Lopez, L. Mangolini, Low activation energy for the crystallization of amorphous silicon nanoparticles, Nanoscale 6 (3) (2014) 1286–1294, https://doi.org/10.1039/c3nr02526h.
[36] Y. Li, J. Li, B. Wang, H. Ma, Z. Han, An approach to the induced reaction mechanism of the combustion of the nano-Al/PVDF composite particles, Surf. Coat. Technol. 429 (2022) 127912, https://doi.org/10.1016/j.surfcoat.2021.127912.
[37] A. Salhi, D.S. Soong, A.T. Bell, The effects of hydrogen on the plasma polymerization of tetrafluoroethylene, Polym. Eng. Sci. 21 (11) (1981) 643–649, https://doi.org/10.1002/pen.760211103.
[38] H. Kobayashi, A.T. Bell, M. Shen, Plasma polymerization of saturated and unsaturated hydrocarbons, Macromolecules 7 (3) (1974) 277–283, https://doi.org/10.1021/ma60039a005.
[39] C.T. Kirk, Quantitative analysis of the effect of disorder-induced mode coupling on infrared absorption in silica, Phys. Rev. B 38 (2) (1988) 1255–1273, https://doi.org/10.1103/PhysRevB.38.1255.
[40] S. Mireja, D.V. Khakhar, Methods to characterize the crystal polymorphs of polyvinylidene fluoride using Fourier transform infrared spectroscopy, Polym. Eng. Sci. 63 (9) (2023) 2857–2870, https://doi.org/10.1002/pen.26410.

[41] S. Uličná, M. Owen-Bellini, S.L. Moffitt, A. Sinha, J. Tracy, K. Roy-Choudhury, D. C. Miller, P. Hacke, L.T. Schelhas, A study of degradation mechanisms in PVDF-based photovoltaic backsheets, Sci. Rep. 12 (1) (2022) 14399, https://doi.org/10.1038/s41598-022-18477-1.
[42] Y. Peng, P. Wu, A two dimensional infrared correlation spectroscopic study on the structure changes of PVDF during the melting process, Polymer 45 (15) (2004) 5295–5299, https://doi.org/10.1016/j.polymer.2004.05.034.
[43] M. Kobayashi, K. Tashiro, H. Tadokoro, Molecular vibrations of three crystal forms of poly(vinylidene fluoride), Macromolecules 8 (2) (1975) 158–171, https://doi.org/10.1021/ma60044a013.
[44] J.E. Castle, Practical surface analysis by Auger and X-ray photoelectron spectroscopy. D. Briggs and M. P. Seah (Editors). John Wiley and Sons Ltd, Chichester, 1983, 533 pp., Surface and Interface Analysis 6(6) (1984) 302-302. 10.1002/sia.740060611.
[45] D. Shi, S.X. Wang, W.J. van Ooij, L.M. Wang, J. Zhao, Z. Yu, Uniform deposition of ultrathin polymer films on the surfaces of Al2O3 nanoparticles by a plasma treatment, Appl. Phys. Lett. 78 (9) (2001) 1243–1245, https://doi.org/10.1063/1.1352700.
[46] A. Tressaud, F. Moguet, S. Flandrois, M. Chambon, C. Guimon, G. Nanse, E. Papirer, V. Gupta, O.P. Bahl, On the nature of C-F bonds in various fluorinated carbon materials: XPS and TEM investigations, J. Phys. Chem. Solids 57 (6) (1996) 745–751, https://doi.org/10.1016/0022-3697(96)00343-5.
[47] H. Groult, D. Devilliers, C. Hinnen, P. Marcus, X-Ray photoelectron spectroscopy of electrogenerated C-F compounds, J. Fluor. Chem. 58 (2) (1992) 284, https://doi.org/10.1016/S0022-1139(00)80740-X.
[48] M. Morita, T. Ohmi, E. Hasegawa, M. Kawakami, M. Ohwada, Growth of native oxide on a silicon surface, J. Appl. Phys. 68 (3) (1990) 1272–1281, https://doi.org/10.1063/1.347181.
[49] A. Kaur, P. Chahal, T. Hogan, Selective fabrication of SiC/Si diodes by excimer laser under ambient conditions, IEEE Electron Device Lett. 37 (2) (2016) 142–145, https://doi.org/10.1109/LED.2015.2508479.
[50] H.H. Park, K.H. Kwon, J.L. Lee, K.S. Suh, O.J. Kwon, K.I. Cho, S.C. Park, Characterization and removal of silicon surface residue resulting from CHF3/C2F6 reactive ion etching, J. Appl. Phys. 76 (8) (1994) 4596–4602, https://doi.org/10.1063/1.357294.
[51] R. Basner, M. Schmidt, E. Denisov, K. Becker, H. Deutsch, Absolute total and partial cross sections for the electron impact ionization of tetrafluorosilane (SiF4), J. Chem. Phys. 114 (3) (2001) 1170–1177, https://doi.org/10.1063/1.1333018.
[52] A.J. de Jesus Silva, M.M. Contreras, C.R. Nascimento, M.F. da Costa, Kinetics of thermal degradation and lifetime study of poly(vinylidene fluoride) (PVDF) subjected to bioethanol fuel accelerated aging, Heliyon 6 (7) (2020) e04573.
[53] G. Jian, S. Chowdhury, K. Sullivan, M.R. Zachariah, Nanothermite reactions: Is gas phase oxygen generation from the oxygen carrier an essential prerequisite to ignition? Combust. Flame 160 (2) (2013) 432–437, https://doi.org/10.1016/j.combustflame.2012.09.009.